tag: sPH-CONF-JET-2025-04
version: 1.0
DOI: unspecified
date: April 5, 2025

sPHENIX Conference Note

...

Underlying event fluctuations and jet background in Au+Au collisions at $\sqrt{s_{NN}} = 200$ GeV with the sPHENIX detector

The sPHENIX Collaboration

Abstract

This sPHENIX Conference Note details the measurement of underlying event (UE) fluctuations and the characterization of calorimeter jet background in Au+Au collision data at nucleon-nucleon center of mass collision energy $\sqrt{s_{NN}} = 200$ GeV collected in 2024 by the sPHENIX experiment. Comparisons are presented of jet-background fluctuations after underlying-event subtraction using three different background-estimation methods. The background-subtraction techniques compared represent a range of commonly used methods, including an iterative η-dependent background estimation, an area-based method, and a multiplicity-based method. The jet-background fluctuations are comparable between the three background-estimation techniques. The fluctuations of the underlying event are determined in minimum bias data by analyzing the energy in windows of the calorimeter system, random cones, reconstructed jets around point-like high-energy probes, and embedded simulated jets. The fluctuations in the UE are found to be primarily driven by stochastic-multiplicity fluctuations and hydrodynamic correlations in particle production.

1 Introduction

The sPHENIX experiment is designed to study the scale-dependent structure of the quark-gluon plasma (QGP) using a broad range of hard probes, including fully reconstructed jets [1, 2]. In order to understand the kinematics of jets produced in these collisions, the large, fluctuating underlying event (UE) of soft particles produced in heavy-ion collisions must be understood and subtracted. The details of the underlying event fluctuations are driven by soft physics, namely from correlations arising from hydrodynamic flow and the shape of single particle spectra [3, 4]. Previous measurements of the UE in calorimeter towers by ATLAS show scaling with event centrality, indicative of short-range correlations and collective flow [5]. Studies of the UE by ALICE found that the fluctuations of UE energy density are well described by a random background with correlations due to hydrodynamic flow and Poisson fluctuations [6]. The average pedestal of the UE can be measured and subtracted from jets on an event-by-event basis using a variety of techniques. The jet background subtraction techniques investigated in this analysis include an iterative method [7], an area-based method [8], and a jet consistent multiplicity-based method [9]. The fluctuations about this pedestal cause over- or under-subtraction resulting in an overall increase in the jet energy resolution, increasing with event centrality. Therefore, understanding the size of these fluctuations is key to understanding the energy resolution of measured jets. This highlights the need for the unfolding of jet measurements using a realistic description of UE fluctuations to correct for the resolution.

This note outlines a measurement of UE fluctuations and characterizations of jet background subtraction techniques in Au+Au collisions at nucleon-nucleon center of mass collision energy $\sqrt{s_{NN}} = 200$ GeV with the sPHENIX detector. The analysis input objects are calibrated towers from the electromagnetic and the inner and outer hadronic calorimeters. The UE pedestal and subtracted fluctuations are reported using calorimeter-window areas and event-by-event energy density (ρ) reconstruction. Jet background fluctuations are characterized by the standard deviation of residual energy $\sigma(\delta E_T)$ for random cones, high-E_T probes, and embedded di-jet events. It is the first measurement of the UE employing a hadronic calorimeter at RHIC and the first direct comparison of jet background subtraction methods used by several of the major experiments in the field.

2 sPHENIX detector

sPHENIX [1, 10] is a new detector designed to measure jet and heavy-flavor probes of the QGP created in Au+Au collisions at the Relativistic Heavy Ion Collider (RHIC) [11]. The tracking system enables precise measurements of heavy-flavor and jet-substructure observables while the electromagnetic and hadronic calorimeter system is used for measuring the energy of jets and identifying direct photons and electrons.

Going outwards starting from the beam line, sPHENIX is comprised of the following subsystems [2]: the MAPS-based Vertex Detector (MVTX); the INTermediate Tracker (INTT); the Time Projection Chamber (TPC) [12]; the Time Projection Chamber Outer Tracker (TPOT) [13]; the Electromagnetic Calorimeter (EMCAL) [14, 15]; the Inner Hadronic Calorimeter (IHCAL) [15]; the 1.4 T superconducting solenoid magnet [16] and the Outer Hadronic Calorimeter (OHCAL) [15].

Except for TPOT, all detectors have full azimuthal coverage and span $|\eta| < 1.1$ in pseudorapidity. sPHENIX also includes a number of forward detectors, namely the Minimum Bias Detectors (MBD), the sPHENIX Event Plane Detectors (sEPD), and the Zero Degree Calorimeters (ZDC) which include the Shower Maximum Detector (SMD).

sPHENIX began its commissioning process in RHIC Run-2023 with Au+Au collisions at $\sqrt{s_{NN}} = 200$ GeV. During RHIC Run-2024, sPHENIX collected a large sample of p+p $\sqrt{s} = 200$ GeV physics data alongside a smaller sample of Au+Au data to complete its commissioning phase in that collision system.

3 Analysis and Results

3.1 Event selection

This analysis uses Au+Au collision data at $\sqrt{s_{NN}}$= 200 GeV collected during a commissioning period in Run-2024. Events are selected by a minimum bias trigger that requires at least two hits on each side of the MBD. Further offline selections, based on the expected correlation between the MBD and ZDC signals, are applied to reject beam backgrounds and non-hadronic interactions. The z-vertex is required to be $|z_{\text{vertex, MBD}}| < 20$ cm. Events within the centrality range 0–80% are considered in the analysis. Approximately one million events are selected for use in this analysis.

3.2 Calorimeter tower reconstruction and calibration

This analysis uses towers from the electromagnetic and both hadronic calorimeters as input objects. The EMCAL energy scale is set using the $\pi^0 \to \gamma\gamma$ mass peak. For the HCAL calibration, the tower-by-tower response to cosmic ray muons is matched between data and simulation. The calibration of the calorimeter systems is detailed in Ref. [17]. HCAL towers correspond to an area of the detector in pseudorapidity (η) and azimuthal angle (ϕ) of $\Delta\eta \times \Delta\phi = 0.1 \times 0.1$. EMCAL towers correspond to an area of $\Delta\eta \times \Delta\phi = 0.025 \times 0.025$. For the iterative-subtraction method used in this analysis, EMCAL towers are combined into pseudo-towers matching the geometry of HCAL. No unfolding was performed for these results, as the objective of the analysis is to inform the unfolding of future jet measurements, therefore results are reported as E_T^{Raw} to signify the transverse energy obtained for the calorimeter towers.

3.3 Simulation samples

Aspects of this analysis use PYTHIA-8 di-jet events, which are then propagated through a full GEANT-4 [18] simulation of the sPHENIX detector and then reconstructed like data. The Detroit PYTHIA-8 tune [19] is used to generate di-jet samples with $\hat{p}_T^{\text{min}} = 10$ and 30 GeV/c with options **HardQCD:all = on** and **PromptPhoton:all = on**. For each Au+Au minimum bias event, one PYTHIA-8 di-jet event is generated with its vertex position shifted to the position from the data event prior to propagating through GEANT-4. The embedding is performed after the full data reconstruction by combining the energies of the towers from the background (data) and simulated (PYTHIA-8) for each calorimeter. Simulated (sim) jets are reconstructed from the towers generated from the PYTHIA-8 and GEANT-4 simulation, whereas reconstructed jets use the reconstructed embedded towers. Sim and reconstructed jets are geometrically matched with $\Delta R = \sqrt{(\eta_s - \eta_r)^2 + (\phi_s - \phi_r)^2} < 0.75R$, where η_s where ϕ_s correspond to the pseudorapidity and azimuthal angle of the sim jet and η_r and ϕ_r correspond to the pseudorapidity and azimuthal angle of the reconstructed jet, respectively.

3.4 Jet Background Subtraction Methods

3.4.1 Iterative-subtraction Method

The iterative-subtraction method is based on Ref. [7], and is motivated by the method used by ATLAS in heavy-ion jet measurements. The UE is determined individually for each layer of the calorimeter in strips of $\Delta\eta = 0.1$. The anti-k_t algorithm [20] is applied to the EMCAL pseudo-towers and inner and outer HCAL towers with a resolution parameter of $R = 0.2$ to determine candidate jets in the event, called "seeds". These seed jets are required to have a maximum constituent tower energy, $E_{T,\mathrm{max}}$, divided by the mean constituent energy, $\langle E_{T,\mathrm{const}} \rangle$, to be greater than three: $E_{T,\mathrm{max}} > 3 \times \langle E_{T,\mathrm{const}} \rangle$. The average energy per tower is determined at constant η, excluding towers within $\Delta R < 0.4$ of a seed from the calculation. The determination is done individually in each of the three calorimeter subsystems. This average energy is then subtracted from each tower in the event, and the collection of $R = 0.2$ jets are updated. For the second iteration, the seeds are required to have a subtracted p_T, $p_{\mathrm{T}}^{\mathrm{sub}} > 7$ GeV. The average energy per tower is again determined, excluding the area around the new set of seeds, and the tower kinematics are updated for the final estimate of the UE. The iterative method has the ability to account directly for flow modulation in the UE, however this component of the subtraction is not included in the studies presented here. These background subtracted towers are then used as input to the fluctuation studies that follow.

3.4.2 Area-Based Subtraction

The area method, as detailed in Ref. [8], is primarily used in STAR and ALICE jet measurements. The method corrects the jet p_T by estimating the average background energy density per unit area. In the area method used here, pseudorapidity dependencies or local fluctuations are not taken into account. The method is expressed as:

$$E_{T,\mathrm{jet}}^{\mathrm{Corr,\,A}} = E_{T,\mathrm{jet}}^{\mathrm{Uncorr.,\,A}} - \rho_{\mathrm{A}} A_{\mathrm{jet}} \tag{1}$$

where $E_{T,\mathrm{jet}}^{\mathrm{Corr,\,A}}$ is the corrected transverse energy of the jet, $E_{T,\mathrm{jet}}^{\mathrm{Uncorr,\,A}}$ is the uncorrected transverse energy, A_{jet} is the area of the jet, and ρ_{A} is the median background energy density, estimated from the median energy density of jets reconstructed with the k_t algorithm with $R = 0.4$ in the event, excluding the two hardest.

3.4.3 Multiplicity-Based Subtraction

The multiplicity method is detailed in Ref. [9]. It is an energy density-based background subtraction method similar to the area-based method. In this approach the average transverse energy of

R	A_{cone}	Window Size	A_{window}
0.2	0.13	3×4	0.11
0.3	0.28	5×6	0.27
0.4	0.5	7×8	0.5
0.5	0.79	9×10	0.81
0.6	1.13	11×12	1.19
0.7	1.54	13×13	1.52
0.8	2.01	15×15	2.02

Table 1: Area of calorimeter window size corresponding to a jet defined by the parameter R.

"background" calorimeter towers and the average tower multiplicity originating from background within the jet are used.

$$E_{T,\text{jet}}^{\text{Corr, N}} = \sum E_{T,\text{tower}} - \rho_{\text{M}}(N_{\text{towers}} - \langle N_{\text{signal}} \rangle), \tag{2}$$

where N_{towers} is the observed number of towers within the jet, $\langle N_{\text{signal}} \rangle$ is the average number of towers in a signal jet of a given $E_{T,\text{jet}}^{\text{raw}}$, and ρ_{M} represents the mean transverse energy per background tower. The N_{towers} parameter is defined as the number of towers which contain energy above threshold. This will be sensitive to the zero-suppression for the case of calorimeter towers. ρ_{M} is determined in a similar way as ρ_{A} but is the median value of the transverse energy per tower among all jets reconstructed with the k_t algorithm with $R = 0.4$, excluding the hardest two in the event.

The average number of particles for jets in proton-proton collisions [21] can adequately described by models meaning $\langle N_{\text{signal}}^{\text{Sim}} \rangle$ can be estimated with accuracy. The value of $\langle N_{\text{signal}}^{\text{Sim}} \rangle$, which is only used in the embedding analysis, is estimated by matching sim PYTHIA-8 jets to the reconstructed embedded jets as described in 3.3. The number of towers in the matched sim jets are binned according to the raw uncorrected E_T of anti-k_t jets reconstructed from the embedding sample, with a requirement that the reconstructed jet energy $E_T^{\text{reco}} > 10$ GeV. The physical EMCAL geometry, rather than the pseudo-towers, is used to increase the dynamic range of the $\langle N_{\text{signal}}^{\text{Sim}} \rangle$ estimation.

3.5 Calorimeter Window Analysis

The calorimeter-window analysis is based on previous studies done by ATLAS [5]. In each event, the calorimeter is divided into $n \times m$ tower-sized windows and the mean and standard deviation of the transverse energy in each of the windows is determined. This is done separately for the EMCAL pseudo-towers (as described in Section 3.2), IHCAL, and OHCAL towers. The final window energy $E_T^{n \times m}$ is the sum of overlapping windows in each of the calorimeter layers. Table 1 shows the correspondence between a given jet radius and a window of approximately the same area. The event-averaged energy $\langle \overline{E_T} \rangle^{n \times m}$ and standard deviation $\bar{\sigma}^{n \times m}$ are used to quantify the average pedestal and fluctuations of the UE.

The correlation of UE fluctuations between calorimeter regions is characterized using the de-

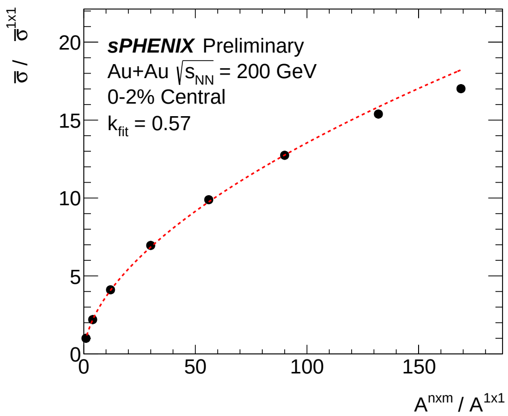

Figure 1: An example of the fit to the formula in Equation 3 for 0–2% central events. The x-axis is scaled by the area of a single tower and the points represent calorimeter-window areas with dimensions presented in Table 1.

pendence of the event-averaged standard deviation $\bar{\sigma}^{n\times m}$ for calorimeter windows with area $A_{\text{window}} = dA_{\text{tower}} \cdot (n \times m)$, where dA_{tower} is the area of a single tower in HCAL geometry ($\Delta\eta \times \Delta\phi$ =0.1 $\times$ 0.1). If the fluctuations are uncorrelated between regions, then $\bar{\sigma}^{n\times m}$ will increase with calorimeter window area proportional to $\sqrt{n \times m}$. Correlated UE fluctuations will cause $\bar{\sigma}^{n\times m}$ to increase faster than $\sqrt{n \times m}$. The dependence of the fluctuations on window area is determined by fitting

$$\bar{\sigma}^{n\times m}/\bar{\sigma}^{1\times 1} = (n \times m)^k, \tag{3}$$

where $\bar{\sigma}^{n\times m}/\bar{\sigma}^{1\times 1}$ is the event-averaged standard deviation scaled by the event-averaged standard deviation for single calorimeter tower windows in a given centrality bin, and k is the correlation parameter. Figure 1 shows examples of these fits for 0–2% central events.

The correlation parameter k is shown for all calorimeter window sizes as a function of event centrality in Figure 2. The simple equation used to extract the correlation parameter k does fails to describe the largest area points in Figure 1. We asses a systematic uncertainty on the extract correlation k_{fit} by removing the two largest area window samples from the fitting range. Varying the range to exclude the window areas where Eq. 3 fails to account for all effects results in less than a 1% effect on the value of k_{fit}. The scaling parameter in peripheral collisions is found to be close to the expected $\sqrt{n \times m}$ scaling, but for central to semi-central collisions the exponent increases to about 0.57 indicating a possible role of correlated fluctuations. The observed scaling faster than $\sqrt{A}$ with respect to centrality could be indicative of short-range correlations and collective flow. Long-range correlations due to flow, and short-range correlations due to hard processes are found to have a dependence on the calorimeter area size. Further study is needed to understand this quantitatively, both in terms of detector response and physics.

3.6 Random Cones Analysis

Random cones allow for the identification of contributions to the fluctuations in terms of jet-like objects without the bias imposed by jet-clustering algorithms [6]. Background fluctuations are sampled by drawing a single rigid cone with radius $R = 0.4$ in a random direction such that the

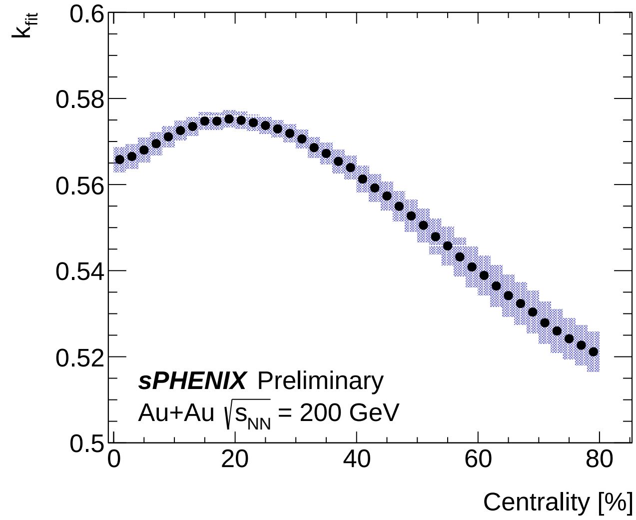

Figure 2: The correlation parameter k from Equation 3 for all fits to the dependence of the mean standard deviation in calorimeter window transverse energy at electromagnetic scale to calorimeter window area, as a function of event centrality. Statistical uncertainties are included. The shaded boxes are the systematic uncertainty from varying the range of fitted window area.

full cone is within calorimeter acceptance $|\eta_{\text{cone}}| < 1.1 - R$, $0 \leq \phi_{\text{cone}} < 2\pi$. Calorimeter towers from the EMCAL, IHCAL, and OHCAL within $\Delta R < 0.4$ of the cone axis are included in the cone energy. The background fluctuations are characterized by the difference in E_T^{Cone} to the average UE pedestal. The expected pedestal is determined using three jet-background subtraction methods described in Section 3.4. The UE fluctuations δE_T for each subtraction method are defined as:

$$\begin{aligned}
\delta E_T^{\text{Area}} &= \sum_{i=0}^{N} E_{T,i} - \rho_{\text{A}} \cdot A_{\text{cone}}, \\
\delta E_T^{\text{Mult}} &= \sum_{i=0}^{N} E_{T,i} - \rho_{\text{M}} \cdot N, \\
\delta E_T^{\text{Iter}} &= \sum_{i=0}^{N} E_{T,i}^{\text{sub}},
\end{aligned} \tag{4}$$

where ρ_{A} and ρ_{M} are the average background densities defined in Section 3.4, $A_{\text{cone}} = \pi R^2$, N is the number of towers within the cone radius, and $E_{T,i}^{\text{sub}}$ is the energy of subtracted-calorimeter towers after iterative subtraction. The multiplicity method is altered in the case of random cone subtraction because $\langle N_{\text{signal}} \rangle$ is assumed to be zero, rather than estimated from the reconstructed cone E_T, due to the assumption that there are no jets present in the minimum bias data.

In addition to static random cones, the analysis is repeated for events in which the tower (η,ϕ) has been randomly moved within the detector. This destroys any event-level angular correlations and allows for a sampling of the underlying-event fluctuations near the expected statistical limit. The two samples of random cones are denoted as “Basic” for standard static random cones, and “Randomized” or “Randomized $\eta\phi$” for random cones constructed with randomized-tower-input objects.

Each δE_T distribution is characterized by the standard deviation $\sigma(\delta E_T)$ for different event centrality bins. The δE_T distributions for random cones subtracted with the area, multiplicity, and iterative subtraction methods in $0-5\%$ central Au+Au events are shown in Figure 3. The distributions have a mean near zero for all methods, indicating each method accurately describes the average UE pedestal.

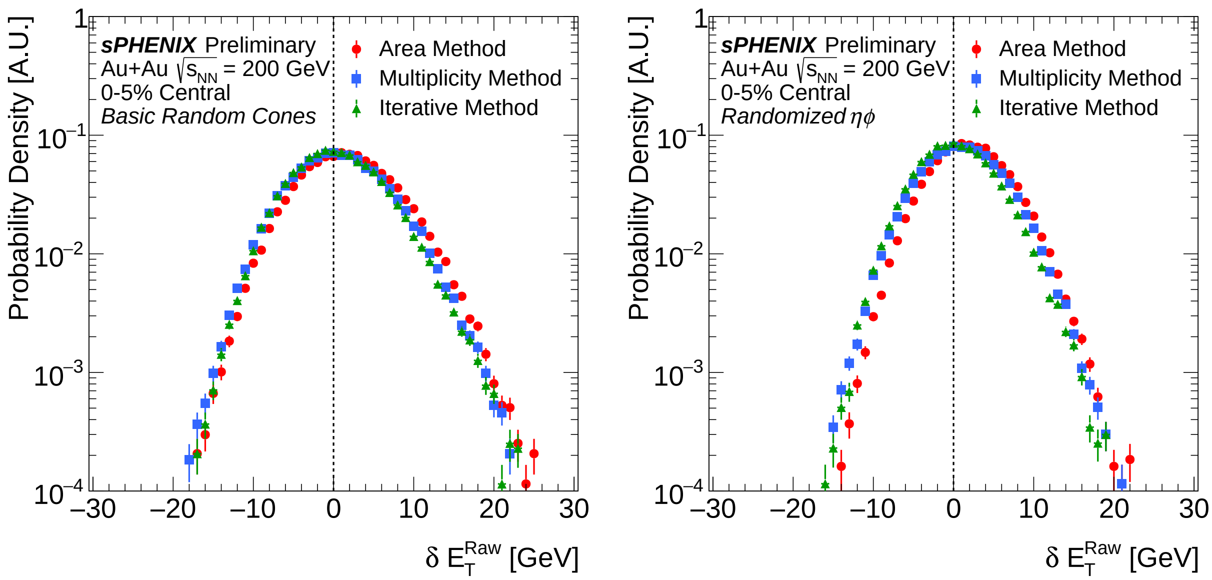

Figure 3: $\delta E_T^{\mathrm{Raw}}$ distributions for random cones reconstructed in 0–5% central events for area-based subtracted (red), multiplicity subtracted (blue), and iteratively subtracted (green) data. The left plot is calculated using random cones constructed with towers in their nominal positions, while the right uses random cones constructed with towers which have had their η and ϕ positions randomized. Values for μ and σ are given in GeV and correspond to the mean and R.M.S of the given distribution.

The dominant contribution to the jet energy resolution in heavy-ion collisions comes from the fluctuations of the UE. The pedestal and fluctuations of the UE, characterized by the ρ-based background subtraction methods, are shown in Figure 4. In the case of random cones where N is the number of towers within the cone and $A = \pi R^2$, both methods are expected to produce similar estimations of the UE. The comparisons of $\rho_{\mathrm{A}} \cdot A$ and $\rho_{\mathrm{M}} \cdot N$ is seen for all centrality classes. The multiplicity-based ρ_{M} can be seen to be systematically greater than the area-based ρ_{A}. This offset is also apparent in Figure 3, where mean value of the δE_T obtained from the multiplicity-based method is ~ 1 GeV less than the mean obtained from the area-based method.

Distributions of UE fluctuations δE_T are characterized by the standard deviation $\sigma(\delta E_T)$ for different event centrality intervals. The δE_T distributions for random cones subtracted with the area, multiplicity, and iterative-subtraction methods in 0–5% central Au+Au events are shown in Figure 5. The distributions are centered near zero for all methods, indicating each method describes the average UE pedestal. The largest discrepancy from a mean value of zero is found for the area method.

The negative tail of the δE_T distributions is fit with a Gaussian function to determine the mean ($\mu^{\mathrm{l.h.s}}$) and standard deviation ($\sigma^{\mathrm{l.h.s}}$) of the left-hand side of the distribution. This Gaussian fit is

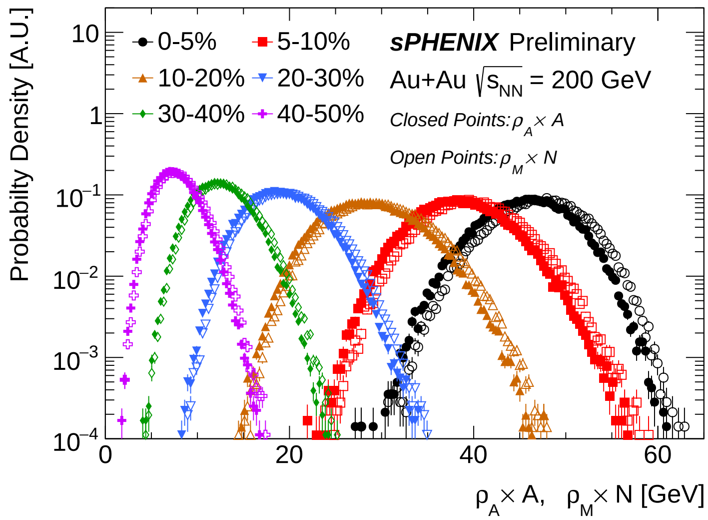

Figure 4: Comparisons of the estimated underlying event distributions for an $R = 0.4$ cone using the multiplicity-based method (open), and the area method (closed) measured in Au+Au events.

extrapolated to positive δE_T for both types of random cones. The positive tail of δE_T is found to be wider than that of a Gaussian distribution for both types of cones. The mean and standard deviation for both types of cones are detailed in Table 2 for 0–5% central Au+Au events. The values for the left-hand side negative δE_T tail are not used in comparisons of underlying-event fluctuations but rather presented to characterize the differences between the positive and negative δE_T tails. The standard deviation for central events using unbiased sampling is found to be $\sigma = 5.69 \pm 0.01$ GeV.

The shape of δE_T is not expected to be Gaussian, even in the limit of purely statistical fluctuations without contributions from hard-scattering or hydrodynamic flow [4, 6, 22]. Approximating this purely statistical limit can be done by randomizing the tower coordinates η and ϕ within an event and calculating the UE fluctuations with the same procedure. This randomization destroys any long-range angular correlations from flow, as well as short-ranged correlations from hard-scattering within the event [9, 22]. Fitting the left-hand side of the δE_T distribution of random cones constructed after randomizing the tower positions and extrapolating to the positive δE_T side shows a disagreement with the positive side data. This shows that even when removing spatial correlations, the distribution has a non-Gaussian positive tail.

The width of the δE_T distribution due to purely statistical fluctuations without event correlations as given in Ref. [6] is:

$$\sigma(\delta E_T) = \sqrt{\langle N \rangle \cdot \langle E_T^2 \rangle}, \tag{5}$$

where $\langle N \rangle$ is the average constituent tower multiplicity for all random cones in events with a given centrality, computed with the basic random cones, and $\langle E_T^2 \rangle = \sigma^2(E_T) + \langle E_T \rangle^2$ is the sum of the variance of single tower energy spectra and the average single tower energy. This expression is derived from the single tower E_T distribution. It is assumed that the single-tower transverse energy spectra are similar in shape to that of the single particle p_T spectra. The contributions of long-range correlations to the UE fluctuations are estimated by including a term that accounts for hydrodynamic flow and any other non-stochastic fluctuation $\sigma_{NS}(\delta E_T)$. Including these effects,

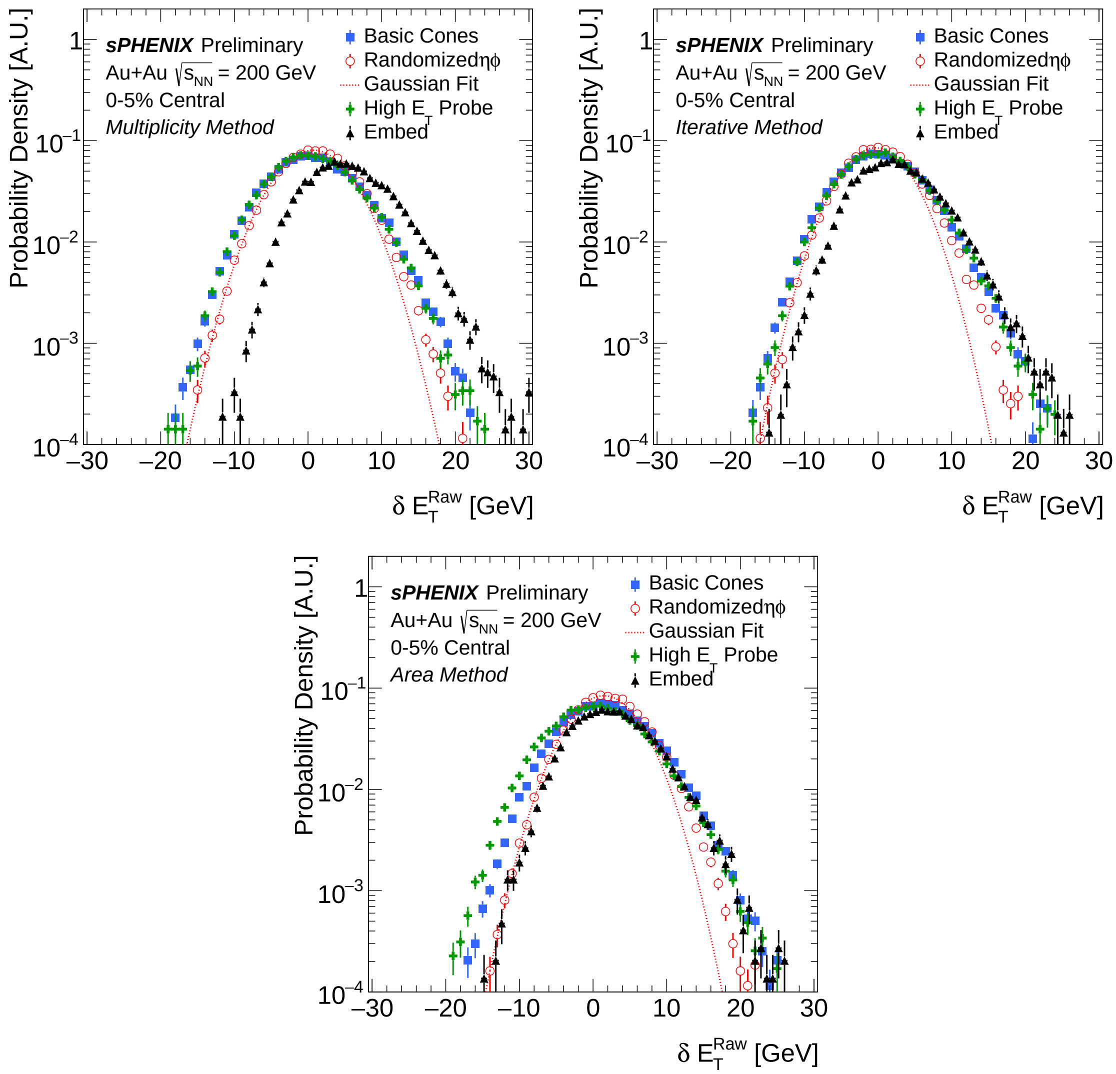

Figure 5: δE_T for multiplicity subtracted (top left), iteratively subtracted (top right), and area subtracted (bottom) underlying-event characterizations in 0–5% central Au+Au events at $\sqrt{s_{NN}}$= 200 GeV for random cones in minimum bias data, both with and without randomizing the tower positions, and in minimum bias data with high-E_T probes and jets embedded in the event. Values for μ and σ are given in GeV and correspond to the mean and R.M.S of the given distribution.

the prediction for the width of δE_T is given by [6]:

$$\sigma(\delta E_T) = \sqrt{\langle N\rangle \cdot \sigma^2(E_T) + \langle N\rangle \cdot \langle E_T\rangle^2 + \sigma^2_{NS}(\delta E_T)}, \tag{6}$$

where previously measured azimuthal anisotropy coefficients, v_n, from STAR are utilized in the estimations for additional multiplicity fluctuations. In Au+Au collisions at $\sqrt{s_{NN}} = 200$ GeV, the elliptical flow v_2 was measured in 0–80% central events [23] and triangular flow v_3 was measured in 0–80% central events [24].

The multiplicity method introduced in Section 3.4.3 was developed for charged-particle jets using tracks as the input object to jet-finding and ρ_M calculations. This method capitalizes on the

	μ [GeV]	σ [GeV]	$\sigma^{\text{l.h.s.}}$ [GeV]	$\mu^{\text{l.h.s.}}$ [GeV]
Area Method				
Basic Cone	1.75 ± 0.03	5.80 ± 0.02	5.15 ± 0.06	0.83 ± 0.12
Randomized $\eta\phi$	2.06 ± 0.02	4.77 ± 0.02	4.38 ± 0.05	1.48 ± 0.08
High-Energy Probe	0.60 ± 0.03	6.08 ± 0.02		
Embedded Jet	2.69 ± 0.04	5.34 ± 0.03		
Multiplicity Method				
Basic Cone	0.71 ± 0.03	5.76 ± 0.02	5.19 ± 0.05	-0.06 ± 0.09
Randomized $\eta\phi$	1.10 ± 0.02	4.97 ± 0.02	4.68 ± 0.05	0.69 ± 0.10
High-Energy Probe	0.58 ± 0.03	5.66 ± 0.02		
Embedded Jet 5.47 ± 0.04	5.47 ± 0.03			
Iterative Method				
Basic Cone	0.46 ± 0.03	5.52 ± 0.02	4.83 ± 0.05	-0.48 ± 0.10
Randomized $\eta\phi$	0.31 ± 0.02	4.77 ± 0.02	4.29 ± 0.05	-0.34 ± 0.08
High-Energy Probe	0.60 ± 0.03	5.47 ± 0.02		
Embedded Jet	2.93 ± 0.04	5.22 ± 0.03		

Table 2: Width and mean of underlying event distributions δE_T and negative δE_T extrapolated via Gaussian fit in 0–5% cental Au+Au events for both types of random cones and embedded high-E_T probes subtracted with each background subtraction method. Values for μ and σ correspond to the mean and R.M.S of the given distribution, while $\sigma^{\text{l.h.s.}}$ $\mu^{\text{l.h.s.}}$ correspond to the mean and standard deviation of the left hand side of the distribution.

fact that the extrinsic variable in the standard deviation is the number of background particles, eliminating the second and third terms in Equation 6. In the case of calorimeter towers as the input to jet-finding, the dynamic range of the jet and cone constituent multiplicity is significantly decreased due to the high occupancy of calorimeters in Au+Au events. The finite tower area can result in multiple particles depositing energy within a tower, especially in high occupancy events.

Figure 6 compares the centrality dependence of $\sigma(\delta E_T)$ for the random cone and randomized $\eta\phi$ methods. The distribution of purely statistical fluctuations, as described by Equation 5, accurately represents the events with randomized tower $\eta\phi$ for all background subtraction methods.

Two curves are predicted to quantify the contributions from higher-order azimuthal anisotropies, according to Equation 6. The elliptical flow contribution is estimated by

$$\sigma_{\text{NS}}^2 \approx 2v_2^2\langle N\rangle^2, \tag{7}$$

where v_2 is the second order flow harmonic [6]. This approximate inclusion of v_2 effects quali-

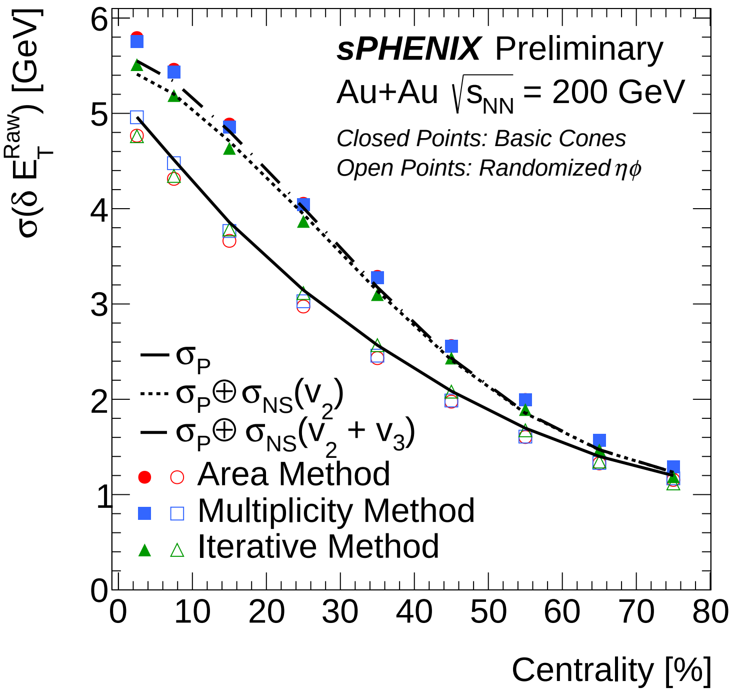

Figure 6: Centrality dependence of $\sigma(\delta E_T)$ of both types of random cones for all background subtraction methods, compared to the Poissonian limit calculated with measured $E_{T,\text{Tower}}$ and to that plus additional hydrodynamic flow contributions calculated with elliptical flow v_2 measured in [23] and triangular flow measured in [24]. The solid black line corresponds to the Poissonian limit given by Eq. 5. The dotted and dashed black lines correspond to estimations of the Poissonian (σ_P) and non-stochastic (σ_{NS}) contributions given by Eq. 7 and Eq. 8, respectively.

tatively accounts for the increased fluctuations observed in mid-central collisions compared to randomized tower $\eta\phi$ events. The triangular flow v_3 contribution is estimated by

$$\sigma_{\text{NS}}^2 \approx 2\langle N\rangle^2(v_2^2 + v_3^2), \tag{8}$$

where v_2 and v_3 are the second and third order flow harmonics, respectively [6]. The inclusion of v_3 effects has minimal impact on the predicted fluctuations for the increased fluctuations observed in central collisions compared to randomized tower $\eta\phi$ events. The positive δE_T tail includes contributions from real hard-scatterings which cannot be separated from the multiplicity fluctuations caused by flow. The discrepancies between the $\sigma(\delta E_T)$ calculated in events with randomized tower $\eta\phi$ and the predicted limit due to purely statistical fluctuations seen in Figure 6 is due to the fact that Equation 5 does not take into account any correlated changes to $\langle E_T\rangle$ due to long-range correlations.

The three background subtraction methods appear to perform similarly in both the basic random cones and for random cones reconstructed in events with randomized tower $\eta\phi$. All methods agree well with each other, with the largest deviations seen in central events up to 0.5 GeV, for both the basic and randomized random cones. The iterative method is able to suppress long-range correlations due to flow better than the event-averaged ρ based methods. To investigate this further, the ratio of UE fluctuations for each method (in both the basic random cones and random cones reconstructed in events with randomized tower $\eta\phi$) to the statistical limit calculated in Equation 5 is determined. Figure 7 shows these ratios for both types of random cones.

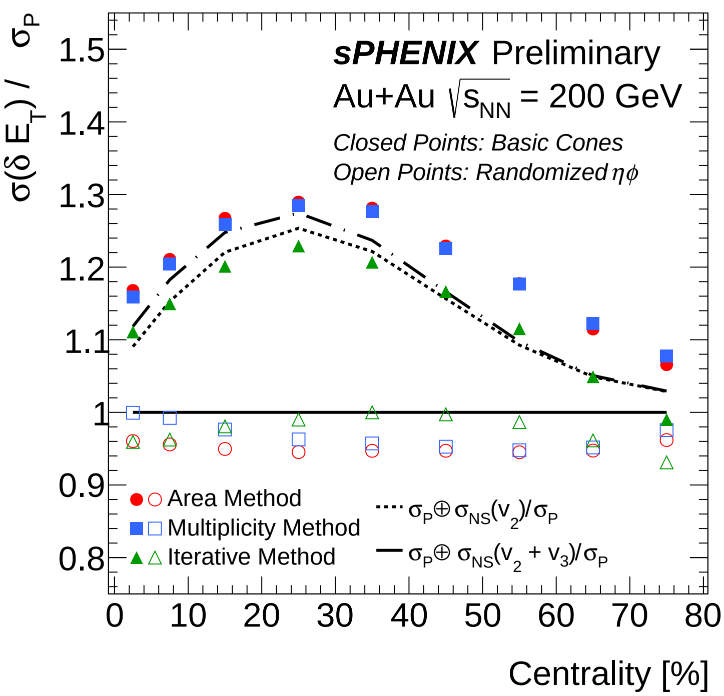

Figure 7: Ratio of $\sigma(\delta E_T)$ to stochastic fluctuations σ_P given by Eq. 5. The fractional contributions to underlying event fluctuations $\sigma(\delta E_T)$ for random cones subtracted with each background subtraction method are shown via Eq. 6. The Poisson (statistical) limit is used as a scale.

The random cones reconstructed in events with randomized tower $\eta\phi$ all are within 5% of unity to the distribution of purely statistical fluctuations, as described by Equation 5, showing that this description accurately represents the events with randomized tower $\eta\phi$ for all background subtraction methods.

The iterative method best describes non-statistical fluctuations due to upward multiplicity fluctuations from flow. There is a constant 5% decrease in the width of UE fluctuations characterized by the iterative method compared to those characterized by the area and multiplicity methods, which is seen in all event-centrality classes. This is due to the nature of the area and multiplicity methods, which estimate the average UE density within an event in a pseudorapidity window of $\Delta\eta = 2.2$, while the iterative method estimates the average underlying-event density in slices of pseudorapidity $\Delta\eta$ = 0.1. This gives the iterative method a better description of the regional fluctuations in multiplicity caused by flow.

3.7 Probe and Jet embedding Analysis

The jet probe analysis quantifies the UE in jets clustered around a point-like massless probe, including the effects of jet reconstruction on the UE, but without the effect of a realistic jet. Additionally, the effects of realistic jets are studied by embedding simulated jets from PYTHIA-8 into minimum bias Au+Au data as described in 3.3. The resulting reconstructed $R = 0.4$ anti-k_t jets which match to the probe or embedded sim jets are studied and their kinematics are compared to that of the embedded probe or jet. In the case of the probe analysis, reconstructed jets are directly matched to the embedded probe, whereas in the embedding case the reconstructed jet is geometrically matched as previously described in 3.3. The δE_T residual is calculated for each of the background subtraction methods according to

$$\begin{aligned}
\delta E_{T,\text{Area}} &= E_{T,\text{jet}}^{\text{Uncorr.}} - \rho_{\text{A}} \cdot A_{\text{jet}} - E_{T,\text{sim}}, \\
\delta E_{T,\text{Mult}} &= E_{T,\text{jet}}^{\text{Uncorr.}} - \rho_{\text{M}} \cdot (N_{\text{const}} - \langle N_{\text{signal}} \rangle) - E_{T,\text{sim}}, \\
\delta E_{T,\text{Iter}} &= E_{T,\text{jet}}^{\text{sub.}} - E_{T,\text{sim}},
\end{aligned} \tag{9}$$

where the A_{jet} is defined using the FASTJET package [25], $\langle N_{\text{signal}} \rangle$ is the expectation value of the number of signal towers in the jet as described in 3.4.3, $E_{T,\text{jet}}^{\text{sub.}}$ is the reconstructed jet from the iteratively subtracted calorimeter towers, and $E_{T,\text{sim}}$ is the energy of either the high-E_T probe or the energy of the matched sim jet. For the jet embedding case, the leading four jets (instead of two) are removed when determining the median area and multiplicity densities to account for the additional two jets. The $\langle N_{\text{signal}} \rangle$ is equal to unity in the E_T probes case, and $\langle N_{\text{signal}} \rangle = \langle N_{\text{PYTHIA-8}} \rangle$, i.e., the mean tower multiplicity in PYTHIA-8. The multiplicity method presented in Ref [9] was developed for charged particle jets. In this analysis we use calorimeter towers, rather than charged particle tracks. The dynamic range for estimating the number of signal towers is limited by the high occupancy of the hadronic calorimeters observed in minimum bias Au+Au events. Therefore the results for the multiplicity method in the case of embedded PYTHIA-8 di-jet events will be skewed to under subtraction.

Probes with $E_{T,\text{probe}} = 30$ GeV are used for the high-E_T input probe. This is done by adding energy randomly within $|\eta_{\text{probe}}| < 0.6$, such that the full $R = 0.4$ reconstructed jet lies within the calorimeter acceptance, after tower calibration and iterative tower subtraction in the case of $E_{T,\text{Iter}}$. Because the energy is placed in a single tower, effects arising from the fragmentation of realistic jets which can cause multiple jets within a single cone are not present. Therefore, the resulting reconstructed jets are always highly circular with radius $\approx R$. Figure 8 (left) shows the δE_T distributions for reconstructed jets that contain a probe $E_{T,\text{probe}} = 30$ GeV in 0–5% central events. The distribution of δE_T is consistent between the three subtraction methods, similar to what was seen with the random cone analysis.

The embedding analysis uses PYTHIA-8 dijet events at $\sqrt{s_{NN}}$ = 200 GeV embedded into minimum bias Au+Au data to evaluate the performance of the separate UE subtraction methods in the presence of more realistic jet objects, the details of which are in 3.3. Selections on the sim jet $E_{T,\text{sim}} > 5$ GeV and unsubtracted reconstructed jet $E_{T,\text{jet}}^{\text{Reco}} > 10$ GeV are applied. Each UE subtraction method is then applied to the reconstructed jets. Figure 8 (right) shows the δE_T distributions for jets reconstructed and matched to an embedded PYTHIA-8 jet. The embedded jets introduce a shift to the mean of the δE_T distributions for the Area and Multiplicity methods, demonstrating potential biases from jet energy on the underlying event calculation.

Figure 5 shows the δE_T distributions for the embedded high E_T probes and PYTHIA-8 jets compared to the random cones and the corresponding mean and width are shown in Table 2. The δE_T of high E_T probes is generally consistent with that from random cones. The presence of embedded

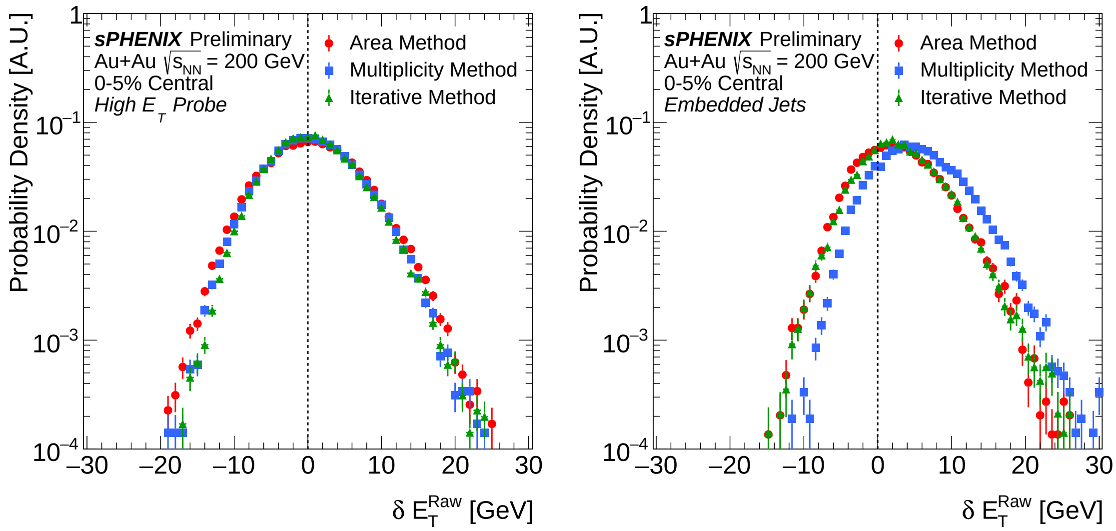

Figure 8: δE_T distributions for jets reconstructed in events with $E_{T,\text{probe}} = 30$ GeV probe (left) embedded PYTHIA-8 event (right). Both panels are for 0–5% central events and show the results of the area-based subtracted (red), multiplicity subtracted (blue), and iteratively subtracted (green) jets.

PYTHIA-8 events cause an increase in the width of δE_T when using the Area and Multiplicity methods, while the same effect is not present in the Iterative method. The presence of the PYTHIA-8 jet also leads to small variations of the mean δE_T on the order of $1-2$ GeV with the largest effect seen in the Area Method.

4 Conclusion

This analysis presents the first measurements of jet background and UE fluctuations from the sPHENIX detector. The UE was characterized in Au+Au collisions at $\sqrt{s_{NN}} = 200$ GeV using windows of the calorimeter with random cones, reconstructed jets around point-like high-energy probes, and embedded-simulated jets. Both long-range correlations due to flow, and short-range correlations due to hard processes were found to have a dependence on the calorimeter area size. The contributing sources to UE fluctuations were determined to be statistical-multiplicity fluctuations and upward-multiplicity correlations due to flow. Long-range correlations from flow comprise up to 30% of UE fluctuations in semi-central Au+Au collisions, steadily decreasing in more peripheral collisions. These findings are broadly consistent with similar studies at the LHC [6, 26], and are quantitatively established here for RHIC energies.

The performance of three jet-background-subtraction methods was assessed by their abilities to suppress UE fluctuations [8, 9, 7]. While all methods were able to reliably estimate the UE pedestal on an event-by-event basis, it was found that upward fluctuations in multiplicity are best suppressed with background-subtraction methods that take local fluctuations into account in their estimates of UE density. These methods account for an increase in the width of the E_T distribution of random cones. The multiplicity method [9], when applied to calorimeter towers instead of charged-particle tracks has a worse performance, which may be improved with the future inclusion of tracking information in jet reconstruction. The iterative method was found to account for upward multiplicity fluctuations from flow better than the other methods. These results will inform the jet reconstruction procedure and the unfolding of jet measurements in sPHENIX.

References

[1] A. Adare *et al* (PHENIX Collaboration). An Upgrade Proposal from the PHENIX Collaboration. 2015. arXiv:1501.06197. 1, 2

[2] The sPHENIX Collaboration. sPHENIX Technical Design Report, PD-2/3 Release, 2019. URL: https://indico.bnl.gov/event/7081/attachments/25527/38284/sphenixtdr20190513.pdf. 1, 2

[3] Sergei A. Voloshin, Arthur M. Poskanzer, and Raimond Snellings. Collective phenomena in non-central nuclear collisions. *Landolt-Bornstein*, 23:293–333, 2010. arXiv:0809.2949, doi:10.1007/978-3-642-01539-7_10. 1

[4] M.J. Tannenbaum. The distribution function of the event-by-event average pt for statistically independent emission. *Physics Letters B*, 498(1):29 – 34, 2001. doi:10.1016/S0370-2693(00)01325-3. 1, 3.6

[5] ATLAS Collaboration. Transverse energy fluctuations in Pb+Pb collisions at $\sqrt{s_{\mathrm{NN}}} = 2.76$ TeV with the ATLAS detector at the LHC. ATLAS-CONF-2012-045, 2012. URL: https://cds.cern.ch/record/1440894. 1, 3.5

[6] B. Abelev *et al* (ALICE Collaboration). Measurement of Event Background Fluctuations for Charged Particle Jet Reconstruction in Pb-Pb collisions at $\sqrt{s_{NN}} = 2.76$ TeV. *JHEP*, 03:053, 2012. arXiv:1201.2423, doi:10.1007/JHEP03(2012)053. 1, 3.6, 3.6, 3.6, 3.6, 3.6, 4

[7] J. A. Hanks, A. M. Sickles, B. A. Cole, A. Franz, M. P. McCumber, D. P. Morrison, J. L. Nagle, C. H. Pinkenburg, B. Sahlmueller, P. Steinberg, M. von Steinkirch, and M. Stone. Method for separating jets and the underlying event in heavy ion collisions at the bnl relativistic heavy ion collider. *Phys. Rev. C*, 86:024908, Aug 2012. URL: https://link.aps.org/doi/10.1103/PhysRevC.86.024908, doi:10.1103/PhysRevC.86.024908. 1, 3.4.1, 4

[8] Matteo Cacciari, Gavin P. Salam, and Gregory Soyez. The Catchment Area of Jets. *JHEP*, 04:005, 2008. arXiv:0802.1188, doi:10.1088/1126-6708/2008/04/005. 1, 3.4.2, 4

[9] Tanner Mengel, Patrick Steffanic, Charles Hughes, Antonio Carlos Oliveira da Silva, and Christine Nattrass. Interpretable machine learning methods applied to jet background subtraction in heavy-ion collisions. *Phys. Rev. C*, 108(2):L021901, 2023. arXiv:2303.08275, doi:10.1103/PhysRevC.108.L021901. 1, 3.4.3, 3.6, 3.7, 4

[10] Ron Belmont et al. Predictions for the sPHENIX physics program. *Nucl. Phys. A*, 1043:122821, 2024. doi:10.1016/j.nuclphysa.2024.122821. 2

[11] M. Harrison, T. Ludlam, and S. Ozaki. RHIC project overview. *Nucl. Instrum. Meth. A*, 499(2):235–244, 2003. doi:10.1016/S0168-9002(02)01937-X. 2

[12] Henry Klest. Overview and design of the sPHENIX TPC. *J. Phys. Conf. Ser.*, 1498:012025, 2020. arXiv:2110.02082, doi:10.1088/1742-6596/1498/1/012025. 2

[13] S. Aune et al. The sPHENIX Micromegas Outer Tracker. *Nucl. Instrum. Meth. A*, 1066:169615, 2024. doi:10.1016/j.nima.2024.169615. 2

[14] C. A. Aidala et al. Design and Beam Test Results for the 2-D Projective sPHENIX Electromagnetic Calorimeter Prototype. *IEEE Trans. Nucl. Sci.*, 68(2):173–181, 2021. doi:10.1109/TNS.2020.3034643. 2

[15] C. A. Aidala *et al* (sPHENIX Collaboration). Design and Beam Test Results for the sPHENIX Electromagnetic and Hadronic Calorimeter Prototypes. *IEEE Trans. Nucl. Sci.*, 65(12):2901–2919, 2018. doi:10.1109/TNS.2018.2879047. 2

[16] T. G. O'Connor et al. Design and testing of the 1.5 T superconducting solenoid for the BaBar detector at PEP-II in SLAC. *IEEE Trans. Appl. Supercond.*, 9:847–851, 1999. doi:10.1109/77.783429. 2

[17] M. I. Abdulhamid et al. Measurement of the transverse energy density in Au+Au collisions at $\sqrt{s_{NN}} = 200$ GeV with the sPHENIX detector. 4 2025. arXiv:2504.02242. 3.2

[18] S. Agostinelli et al. Geant4—a simulation toolkit. *Nuclear Instruments and Methods in Physics Research Section A: Accelerators, Spectrometers, Detectors and Associated Equipment*, 506(3):250–303, 2003. URL: https://www.sciencedirect.com/science/article/pii/S0168900203013688, doi:10.1016/S0168-9002(03)01368-8. 3.3

[19] Manny Rosales Aguilar, Zilong Chang, Raghav Kunnawalkam Elayavalli, Renee Fatemi, Yang He, Yuanjing Ji, Dmitry Kalinkin, Matthew Kelsey, Isaac Mooney, and Veronica Verkest. pythia8 underlying event tune for rhic energies. *Phys. Rev. D*, 105:016011, Jan 2022. URL: https://link.aps.org/doi/10.1103/PhysRevD.105.016011, doi:10.1103/PhysRevD.105.016011. 3.3

[20] M. Cacciari, G. P. Salam, and G. Soyez. The anti-kt jet clustering algorithm. *Journal of High Energy Physics*, 2008(04):063–063, April 2008. URL: http://dx.doi.org/10.1088/1126-6708/2008/04/063, doi:10.1088/1126-6708/2008/04/063. 3.4.1

[21] B. Abelev *et al* (ALICE Collaboration). Charged jet cross sections and properties in proton-proton collisions at $\sqrt{s} = 7$ TeV. *Phys. Rev. D*, 91(11):112012, 2015. arXiv:1411.4969, doi:10.1103/PhysRevD.91.112012. 3.4.3

[22] Charles Hughes, Antonio Carlos Oliveira Da Silva, and Christine Nattrass. Model studies of fluctuations in the background for jets in heavy ion collisions. *Phys. Rev. C*, 106(4):044915, 2022. arXiv:2005.02320, doi:10.1103/PhysRevC.106.044915. 3.6

[23] B. I. Abelev *et al* (STAR Collaboration). Centrality dependence of charged hadron and strange hadron elliptic flow from $\sqrt{s_{\rm NN}} = 200$ GeV Au + Au collisions. *Phys. Rev. C*, 77:054901, 2008. arXiv:0801.3466, doi:10.1103/PhysRevC.77.054901. 3.6, 6

[24] L. Adamczyk *et al* (STAR Collaboration). Third Harmonic Flow of Charged Particles in Au+Au Collisions at $\sqrt{s_{\rm NN}} = 200$ GeV. *Phys. Rev. C*, 88(1):014904, 2013. arXiv:1301.2187, doi:10.1103/PhysRevC.88.014904. 3.6, 6

[25] Matteo Cacciari, Gavin P. Salam, and Gregory Soyez. FastJet User Manual. *Eur. Phys. J. C*, 72:1896, 2012. arXiv:1111.6097, doi:10.1140/epjc/s10052-012-1896-2. 3.7

[26] G. Aad *et al* (ATLAS Collaboration). Measurement of the jet radius and transverse momentum dependence of inclusive jet suppression in lead-lead collisions at $\sqrt{s_{NN}}$= 2.76 TeV with the ATLAS detector. *Phys. Lett. B*, 719:220–241, 2013. arXiv:1208.1967, doi:10.1016/j.physletb.2013.01.024. 4